

Electrical transport near quantum criticality in low dimensional organic superconductors

M. Shahbazi^{1,*} and C. Bourbonnais^{1,†}

¹*Regroupement Québécois sur les Matériaux de Pointe, Département de physique,
Université de Sherbrooke, Sherbrooke, Québec, Canada, J1K-2R1*

(Dated: August 24, 2015)

We propose a theory of longitudinal resistivity in the normal phase of quasi-one-dimensional organic superconductors near the quantum critical point where antiferromagnetism borders with superconductivity under pressure. The linearized semi-classical Boltzmann equation is solved numerically, fed in by the half-filling electronic umklapp scattering vertex as derived from one-loop renormalization group calculations for the quasi-one-dimensional electron gas model. The momentum and temperature dependence of umklapp scattering has an important impact on the behaviour of longitudinal resistivity in the normal phase. Resistivity is found to be linear in temperature around the quantum critical point at which spin-density-wave order joins superconductivity along the antinesting axis, to gradually evolve towards the Fermi liquid behaviour in the limit of weak superconductivity. A comparison is made between theory and experiments performed on the (TMTSF)₂PF₆ member of the Bechgaard salt series under pressure.

PACS numbers: 74.25.fc, 71.10.Hf, 74.70.Kn

I. INTRODUCTION

The quasi-one-dimensional (quasi-1D) organic conductors (TMTSF)₂X, called the Bechgaard salts, are known to be among the first examples of correlated electron systems in which superconductivity (SC) borders with antiferromagnetism or spin-density-wave order (SDW) in their phase diagram¹⁻⁴. Both orderings are brought in close proximity by tuning pressure which can be achieved either hydrostatically or by chemical means. This results in a characteristic SDW-SC sequence of instabilities that shares many common traits with other unconventional superconductors including members of cuprate^{5,6}, heavy-fermion^{7,8}, and pnictide^{8,9} series of compounds. This sequence is typically preceded by a metallic phase with unusual properties. For the Bechgaard salts, an anomalous metallic phase occurs nearby the critical pressure P_c , as a quantum critical point (QCP) connecting the ordering temperature T_c for SC at its optimal value with the vanishing T_{SDW} for SDW^{3,4}. The temperature dependence of longitudinal resistivity near this point is found to depart from the T^2 behaviour for a Fermi liquid. A detailed analysis has revealed that resistivity is instead linear in temperature close to P_c , as commonly found near a QCP⁵. It smoothly evolves toward the Fermi liquid prediction as pressure is tuned away from P_c , in apparent correspondence with the gradual suppression of T_c under pressure^{10,11}.

Generally linked to a QCP with SDW is the presence of spin fluctuations in the metallic state. These fluctuations may give rise to an important source of electron-electron umklapp scattering. As a mechanism of momentum dissipation, umklapp enters as a key determinant in the temperature dependence of resistivity^{12,13}. In systems like the Bechgaard salts, this scattering process is primarily the consequence of a weak dimerization of the organic stacks which imparts a half-filled char-

acter to the electron band and allows the longitudinal transfer of charge carriers across the Fermi surface¹⁴. The existence of SDW fluctuations in the metallic phase of these materials has been amply borne out by NMR measurements¹⁵⁻¹⁹. The temperature dependence of the nuclear spin relaxation rate T_1^{-1} shows a pronounced enhancement of the Curie-Weiss form, at variance with the linear- T Korringa law expected for a Fermi liquid. The amplitude of enhancement is in precise correspondence with the anomalous resistivity and the size of T_c over the broad range of pressure where superconductivity is present^{19,20}, showing an intimate connection between SDW and Cooper pairing.

From a theoretical point of view, one-loop renormalization group (RG) studies on the quasi-1D electron gas model with umklapp scattering have previously shown how the SDW-SC sequence of instabilities can be reproduced by varying the transverse next-to-nearest-neighbour hopping term t'_\perp , which acts as an antinesting term that simulates the role of pressure in the model^{20,21}. Along the antinesting axis, a critical value t'^*_\perp can be defined as the analogue of the actual QCP at P_c . This is where T_{SDW} is suppressed and a d-wave SC (SCd) instability appears at a maximum T_c . The SDW-SCd pattern is also found to be accompanied by SDW fluctuations over a wide temperature domain of the non ordered state. Above t'^*_\perp for instance, the calculated SDW susceptibility in the normal phase fits a Curie-Weiss form in agreement with the one extracted from NMR experiments. This enhancement of SDW correlations is mainly ascribed to the positive response of umklapp scattering to the growth of d-wave pairing^{20,22}.

From the one-loop electron-electron vertex functions obtained for the electron gas, the quasi-particle scattering rate has been computed from the self-energy^{11,22}. Near t'^*_\perp , the rate develops a linear T dependence above T_c , to which a Fermi liquid T^2 component subsequently

adds and grows as t'_\perp distances from the QCP and T_c decreases. This qualitatively agrees with the polynomial T -analysis of resistivity data in systems like $(\text{TMTSF})_2\text{PF}_6$ and $(\text{TMTSF})_2\text{ClO}_4$ over the whole pressure domain where superconductivity is found^{10,11}. An alternative self-energy approach to resistivity data has been proposed from a hot-cold spots picture of the SDW nesting along quasi-1D Fermi surface in the conventional framework of the QCP where superconductivity is neglected²³.

In this work we intend to push the calculation of longitudinal resistivity a step beyond the self-energy approach by solving the semi-classical Boltzmann equation. This is achieved numerically with the aid of the RG method which is employed to compute the momentum and temperature dependent umklapp scattering vertex function entering the collision term of the Boltzmann equation. Our procedure is similar in the outline with the one recently proposed by Buhmann *et al.*,²⁴ in the study of transport properties of the hole-doped cuprate superconductors.

The results put forward below show that resistivity develops a metallic linear- T dependence as antinesting approaches its critical value t'_\perp^* where SDW and SCd orders meet. This quantum critical behaviour in resistivity ensues from the anisotropic growth of half-filling umklapp scattering with lowering temperature, a consequence of reinforcement of commensurate SDW correlations by SCd pairing in the metallic phase, which persists down to T_c . Above t'_\perp^* , the reinforcement undergoes a gradual decline that defines an extended region of quantum criticality where the temperature dependence of resistivity can fit a power law dependence $\rho(T) \sim T^\alpha$ with an exponent $\alpha < 2$. The exponent approaches the Fermi liquid limit $\alpha \simeq 2$ at low enough temperature and for sufficiently large t'_\perp , namely where T_c becomes small. Anisotropy developed by umklapp scattering is found to have a sizeable impact on the momentum dependence of the scattering rate extracted from resistivity.

The linearized Boltzmann transport theory is introduced in Sec. II and Appendix A. In Sec. III and Appendix B, we present the RG approach of the quasi-1D electron gas, from which the results for the phase diagram along with the temperature and momentum dependence of umklapp scattering vertex entering the Boltzmann equation are given. In Sec. IV, numerical results for resistivity and their analysis in terms of renormalized umklapp vertex function are detailed. A comparison with existing experiments performed on the $(\text{TMTSF})_2\text{PF}_6$ member of the Bechgaard salts is presented. We summarize and conclude this work in Sec. V.

II. BOLTZMANN EQUATION

The semiclassical Boltzmann equation describes the variation of the quasi-particle Fermi distribution function f due to collisions and external forces. In the presence of a spatially uniform and static electric field \mathcal{E} coming from a one-body electrostatic potential, the Boltzmann

equation reduces to the expression

$$\frac{df(\mathbf{k})}{dt} = e\mathcal{E} \cdot \nabla_{\hbar\mathbf{k}} f = \left[\frac{\partial f(\mathbf{k})}{\partial t} \right]_{\text{coll}}, \quad (1)$$

where e is the electric charge. The collision integral for an array of N_P chains of length L takes the form

$$\begin{aligned} \left[\frac{\partial f(\mathbf{k})}{\partial t} \right]_{\text{coll}} &= (LN_P)^{-2} \sum_{\mathbf{k}_2, \mathbf{k}_3, \mathbf{k}_4} w(\mathbf{k}, \mathbf{k}_2; \mathbf{k}_3, \mathbf{k}_4) \\ &\times \{ f(\mathbf{k})f(\mathbf{k}_2)[1 - f(\mathbf{k}_3)][1 - f(\mathbf{k}_4)] \\ &- [1 - f(\mathbf{k})][1 - f(\mathbf{k}_2)]f(\mathbf{k}_3)f(\mathbf{k}_4) \}, \end{aligned} \quad (2)$$

for scattering in and out processes. The electron-electron (longitudinal umklapp) contribution to scattering rate w is obtained from the Fermi golden rule,

$$\begin{aligned} w(\mathbf{k}, \mathbf{k}_2; \mathbf{k}_3, \mathbf{k}_4) &= \frac{1}{2} |\langle \mathbf{k}, \mathbf{k}_2 | g_3 | \mathbf{k}_3, \mathbf{k}_4 \rangle - \langle \mathbf{k}, \mathbf{k}_2 | g_3 | \mathbf{k}_4, \mathbf{k}_3 \rangle|^2 \\ &\times \delta_{\mathbf{k}+\mathbf{k}_2, \mathbf{k}_3+\mathbf{k}_4+\mathbf{G}} \frac{2\pi}{\hbar} \delta(\varepsilon_{\mathbf{k}} + \varepsilon_{\mathbf{k}_2} - \varepsilon_{\mathbf{k}_3} - \varepsilon_{\mathbf{k}_4}) \end{aligned} \quad (3)$$

where $\mathbf{G} = (4k_F, 0)$ is the longitudinal reciprocal lattice vector for half-filling umklapp scattering, and $k_F = \pi/(2a)$ is the longitudinal (1D) Fermi wave vector for dimerized chains.

To linearize the Boltzmann equation, we introduce the normalized deviation function $\phi_{\mathbf{k}}$ in the Fermi distribution function²⁵,

$$f(\mathbf{k}) = \frac{1}{e^{\beta\varepsilon_{\mathbf{k}}^p - \phi_{\mathbf{k}} + 1}}, \quad (4)$$

where $\beta = 1/T$ ($k_B = 1$). The electron energy spectrum is the one of the quasi-1D electron gas model

$$\varepsilon_{\mathbf{k}}^p = \hbar v_F(pk - k_F) + \varepsilon_\perp(k_\perp). \quad (5)$$

The spectrum comprises a longitudinal part linearized around the right/left 1D Fermi points $pk_F = \pm k_F$ with v_F as the longitudinal Fermi velocity. The transverse part is given by

$$\varepsilon_\perp(k_\perp) = -2t_\perp \cos k_\perp d_\perp - 2t'_\perp \cos 2k_\perp d_\perp, \quad (6)$$

where t_\perp and t'_\perp are the first and second nearest-neighbour interchain hopping terms and d_\perp is the interchain distance.

The first order expansion $f(\mathbf{k}) \simeq f^0(\mathbf{k}) + f^0(\mathbf{k})[1 - f^0(\mathbf{k})]\phi_{\mathbf{k}}$ of the distribution function yields after substitution in (1),

$$\mathcal{L}\phi_{\mathbf{k}} = e\beta\mathcal{E} \cdot v_{\mathbf{k}}, \quad (7)$$

where $\mathcal{E} \sim \mathcal{O}(\phi)$. This is the linearized Boltzmann equation in which the collision operator \mathcal{L} obeys the relation

$$\mathcal{L}\phi_{\mathbf{k}} = \sum_{\mathbf{k}'} \mathcal{L}_{\mathbf{k}, \mathbf{k}'} \phi_{\mathbf{k}'}. \quad (8)$$

The matrix elements are of the form

$$\begin{aligned} \mathcal{L}_{\mathbf{k},\mathbf{k}'} = & \frac{1}{(LN_P)^2} \sum_{\mathbf{k}_2, \mathbf{k}_3, \mathbf{k}_4} \frac{1}{2} |\langle \mathbf{k}, \mathbf{k}_2 | g_3 | \mathbf{k}_3, \mathbf{k}_4 \rangle - \langle \mathbf{k}, \mathbf{k}_2 | g_3 | \mathbf{k}_4, \mathbf{k}_3 \rangle|^2 \frac{2\pi}{\hbar} \delta_{\mathbf{k}+\mathbf{k}_2, \mathbf{k}_3+\mathbf{k}_4+p\mathbf{G}} \delta(\varepsilon_{\mathbf{k}}^p + \varepsilon_{\mathbf{k}_2}^{p_2} - \varepsilon_{\mathbf{k}_3}^{p_3} - \varepsilon_{\mathbf{k}_4}^{p_4}) \\ & \times \frac{f^0(\mathbf{k}_2)[1-f^0(\mathbf{k}_3)][1-f^0(\mathbf{k}_4)]}{[1-f^0(\mathbf{k})]} (\delta_{\mathbf{k},\mathbf{k}'} + \delta_{\mathbf{k}_2,\mathbf{k}'} - \delta_{\mathbf{k}_3,\mathbf{k}'} - \delta_{\mathbf{k}_4,\mathbf{k}'}) = \sum_{i=1}^4 \mathcal{L}_{\mathbf{k},\mathbf{k}'}^{[i]}, \end{aligned} \quad (9)$$

which separates into a diagonal ($\mathcal{L}^{[1]}$) and three off-diagonal terms ($\mathcal{L}^{[2-4]}$). In the Appendix A, each term is evaluated explicitly in the framework of the quasi-1D electron gas model introduced in Sec. III.

For an electric field $\mathcal{E} = \mathcal{E}_a \hat{a}$ oriented along the chain direction, the corresponding electrical current density $j_a = \sigma_a \mathcal{E}_a$ allows us to extract the conductivity σ_a , as the inverse of longitudinal resistivity ρ_a . To first order in ϕ , the current density is given by

$$\begin{aligned} j_a = & \frac{2e}{LN_P d_{\perp}} \sum_{\mathbf{k}} v_F f(\mathbf{k}) \\ \simeq & \frac{2e}{LN_P d_{\perp}} \sum_{\mathbf{k}} v_F f^0(\mathbf{k}) [1 - f^0(\mathbf{k})] \phi_{k_{\perp}}. \end{aligned} \quad (10)$$

Since for all temperatures of interest, the product $f^0[1 - f^0]$ is strongly peaked at the Fermi level, the deviation $\phi_{\mathbf{k}} \rightarrow \phi_{\mathbf{k}_F^p} \equiv \phi_{k_{\perp}}$ can be evaluated at the Fermi wave vector $\mathbf{k}_F^p = (k_F^p(k_{\perp}), k_{\perp})$, whose location on the p Fermi surface sheet is entirely parametrized by k_{\perp} from the equation $\epsilon_{\mathbf{k}_F^p}^p = 0$. By introducing the normalized deviation $\bar{\phi}_{k_{\perp}} = \phi_{k_{\perp}} / (\beta e \mathcal{E}_a d_{\perp})$ and after an energy integration following (A4), the 2D conductivity or the inverse resistivity in the longitudinal direction becomes

$$\sigma_a = \rho_a^{-1} = \frac{e^2}{\hbar} \langle \bar{\phi}_{k_{\perp}} \rangle_{\text{FS}}, \quad (11)$$

where $\langle \bar{\phi}_{k_{\perp}} \rangle_{\text{FS}} = 1/N_P \sum_{k_{\perp}} \bar{\phi}_{k_{\perp}}$ is the deviation function averaged over the Fermi surface. The function $\bar{\phi}_{k_{\perp}}$ satisfies the equation

$$\sum_{i, k'_{\perp}} \bar{\mathcal{L}}_{k_{\perp}, k'_{\perp}}^{[i]} \bar{\phi}_{k'_{\perp}} = 1, \quad (12)$$

whose explicit expression is given in (A6) and for which we have introduced the dimensionless operator $\bar{\mathcal{L}}^{[i]} = \frac{\pi d_{\perp}}{v_F} \mathcal{L}^{[i]}$. The above expression is fed by the momentum and temperature dependence of the umklapp vertex function. This function is provided by the RG approach to the quasi-1D electron gas model that is introduced next.

III. RENORMALIZED UMKLAPP SCATTERING FOR THE ELECTRON GAS MODEL

A. The model

The quasi-1D electron gas model in its standard form comprises, besides its one-electron energy spectrum (5),

three electron-electron coupling constants that will be defined here on the Fermi surface sheets \mathbf{k}_F^p . These are the backward and the forward scattering amplitudes $g_1(\mathbf{k}_{F,1}^-, \mathbf{k}_{F,2}^+; \mathbf{k}_{F,3}^-, \mathbf{k}_{F,4}^+)$ and $g_2(\mathbf{k}_{F,1}^+, \mathbf{k}_{F,2}^-; \mathbf{k}_{F,3}^-, \mathbf{k}_{F,4}^+)$ for normal scattering processes between right and left moving carriers, and $g_3(\mathbf{k}_{F,1}^p, \mathbf{k}_{F,2}^p; \mathbf{k}_{F,3}^p, \mathbf{k}_{F,4}^p)$ for umklapp scattering along the chains, whose momentum conservation involves the reciprocal lattice vector $\mathbf{G} = (4k_F, 0)$ at half-filling. These coupling constants can be seen as phenomenological parameters of the model whose range at the bare level can be fixed from experimental data. We will follow²⁰⁻²², and use the typical values (normalized by $\hbar\pi v_F$), $g_1 \simeq 0.32$ and $g_2 \simeq 0.64$ for the two normal processes, consistent with the observed enhancement of uniform magnetic susceptibility²⁶ and the scale of T_{SDW} at low pressure^{27,28}. As for the umklapp term, its bare value is primarily proportional to the dimerization gap Δ_D ²⁹ of the organic stacks ($g_3 \approx g_1 \Delta_D / E_F$)^{30,31}, which is small in the Bechgaard salts. Although rather weak at the bare level, umklapp processes have a strong influence on spin fluctuations at low energy and enter as a key determinant in the temperature dependence of longitudinal resistivity as we will see. The bare umklapp amplitude will thus be varied in the interval $g_3 \simeq 0.02 \dots 0.035$, in accordance with the range of values expected for Δ_D ²⁹. For the model spectrum (5), we shall use $E_F = 3000\text{K}$ and $t_{\perp} = 200\text{K}$ for the Fermi energy and transverse hopping, as representative figures of the band structure for the Bechgaard salts^{32,33}. The transverse second nearest-neighbour hopping t'_{\perp} , which introduces nesting alterations, will be varied continuously to simulate pressure effects.

We follow the lines of previous works and apply the Kadanoff-Wilson RG approach to the quasi-1D electron gas model which is outlined in Appendix B^{21,22,34,35}. Each constant energy surface is first divided into $N_P (= 60)$ patches, each centered on a discrete value of k_{\perp} parametrizing each Fermi sheet $\mathbf{k}_F^p = (k_F^p(k_{\perp}), k_{\perp})$. The successive integration of electronic degrees of freedom as a function of the energy distance from the Fermi surface comprises perturbative contributions to the scattering amplitudes coming from closed loops, vertex corrections and ladder diagrams of the density-wave (Peierls) and electron-electron (Cooper) scattering channels. The resulting RG flow equations for the k_{\perp} -dependent scattering amplitudes $g_{1,2,3}(k_{\perp 1}, k_{\perp 2}; k_{\perp 3}, k_{\perp 4})$ on the Fermi surface are reproduced in (B1) of Appendix B. Their k_{\perp} dependence takes into account the transverse momentum variables in both Peierls and Cooper channels, along with the longitudinal momentum transfer in each chan-

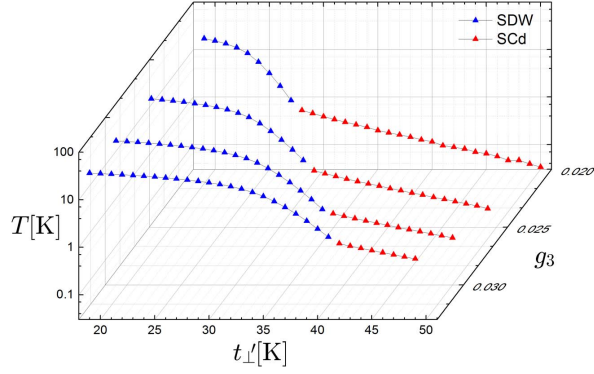


FIG. 1. (Color online) Calculated phase diagram of the quasi-one-dimensional electron gas model showing the SDW-SCd sequence of instabilities as a function of antineesting t'_\perp and initial g_3 .

nel which is adjusted so that the momentum of ingoing and outgoing particles fall on the warped Fermi surface.

These flow equations are completed by those of the susceptibilities $\chi_\mu(\mathbf{q}_0)$ given in (B4). These serve to signal an instability against either $\mu = \text{SDW}$ or $\mu = \text{SCd}$ types of ordering at the corresponding wave vectors $\mathbf{q}_0 = (2k_F, \pi)$ and $\mathbf{q}_0 = 0$.

B. The phase diagram

The integration of the flow equations for the scattering amplitudes (B1) and susceptibilities (B4-B5) leads to their corresponding renormalized values at temperature T . For the above set of model parameters, the singularities in $\chi_{\text{SDW}}(2k_F, \pi)$ and $\chi_{\text{SCd}}(0)$ at temperatures T_{SDW} and T_{SCd} enable to follow the SDW-SCd sequence of instabilities as a function of the antineesting parameter t'_\perp and initial g_3 . The resulting phase diagrams are shown in Fig. 1. The variation of T_{SDW} shows a characteristic monotonic decrease with t'_\perp up to the approach of the critical value t'^*_\perp where T_{SDW} undergoes a rapid decrease, followed by the emergence of a SCd instability. The latter reaches its maximum T_c at t'^*_\perp , followed by its steady decrease for larger t'_\perp . The impact of increasing the initial g_3 on this sequence is to magnify antiferromagnetism and T_{SDW} , which ultimately translates into an increase of the critical t'^*_\perp and an enhancement of d-wave Cooper pairing, as shown by the upward shift of the T_c line in Fig. 1.

C. Umklapp scattering

In the SDW sector of the phase diagram, the umklapp scattering amplitude g_3 develops like χ_{SDW} a singular growth at the approach of T_{SDW} . For $t'_\perp < t'^*_\perp$ and different temperatures, Fig. 2-a shows the contour plot

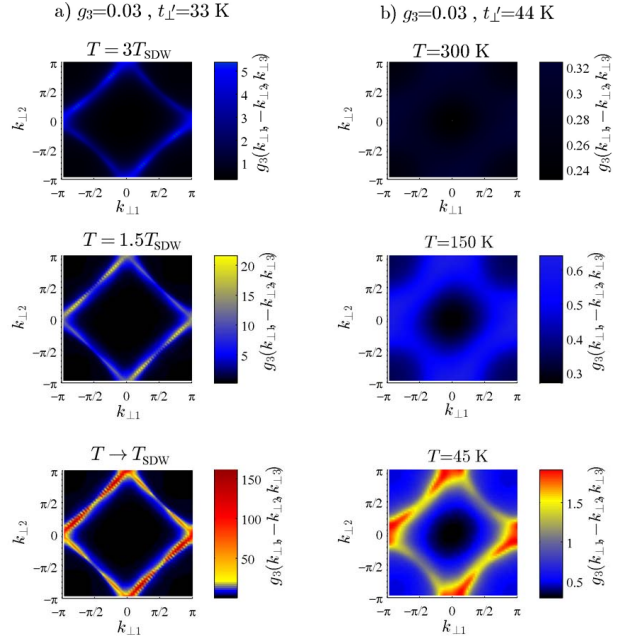


FIG. 2. Renormalized umklapp scattering amplitude projected in the $(k_{\perp 1}, k_{\perp 2})$ plane in the normal phase at different temperatures for the initial $g_3 = 0.03$ ($t'^*_\perp = 38\text{K}$). (a): $t'_\perp = 33\text{K}$ ($< t'^*_\perp$); (b): $t'_\perp = 44\text{K}$ ($> t'^*_\perp$).

of $g_3(k_{\perp 1}, -k_{\perp 1}, k_{\perp 2})$ projected in the $(k_{\perp 1}, k_{\perp 2})$ plane at zero transverse momentum for the pairs of ingoing and outgoing particles. As shown in the Figure 2-a, the maximum of scattering intensity is mainly concentrated along the lines $k_{\perp 2} = k_{\perp 1} \pm \pi$, which is congruent with the transverse component of the SDW correlation wave vector $\mathbf{q}_0 = (2k_F, \pi)$. Along these lines, the singular growth is the strongest around the spots $(0, \pm\pi)$ and $(\pm\pi, 0)$, whose components differ from the points $k_\perp = \pm\pi/4, \pm 3\pi/4$ on the Fermi surface where nesting is predicted to be optimal for the spectrum (5). The fact that the warmest regions of scattering on the Fermi surface differ from the nesting prediction reflects the influence of Cooper scattering channel in the anisotropic flow of g_3 in Eq. (B1).

If we now consider the low temperature variation of umklapp in the SCd sector of the phase diagram at $t'_\perp > t'^*_\perp$, we note according to Fig. 3 that g_3 is no longer singular for all temperatures down to T_c . However, as temperature is decreasing we still observe an enhancement of g_3 along the SDW lines of scattering $k_{\perp 2} = k_{\perp 1} \pm \pi$. These are associated with peaks at $k_\perp = 0, \pm\pi$ on the Fermi surface whose amplitude increases with the bare g_3 , as shown in Fig. 3. According to the combination $g_{\text{SDW}} = g_2 + g_3$ of couplings entering in the SDW susceptibility [see Eq. (B6)], a positive increase in umklapp goes hand in hand with an increase of SDW spin correlations. This has been shown to yield a temperature dependence for $\chi_{\text{SDW}}(\mathbf{q}_0) \sim 1/(T + \Theta)$ of the Curie-Weiss form in the same temperature domain, with an en-

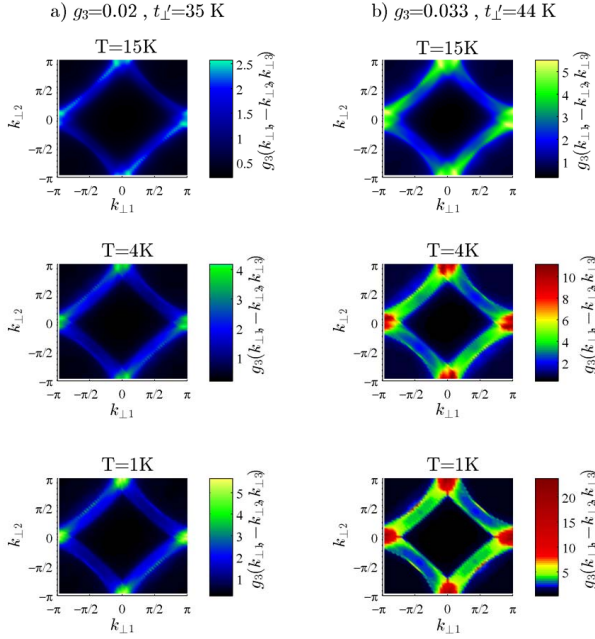


FIG. 3. (Color online) Renormalized umklapp scattering amplitude projected in the $(k_{\perp 1}, k_{\perp 2})$ plane in the normal phase of the SCd sector of the phase diagram, as obtained at different temperatures and initial values of g_3 .

ergy scale Θ for SDW correlations approaching zero at t_{\perp}' and raising linearly with t_{\perp}' from the QCP^{20,22,36}. Occurring despite poor nesting conditions, the enhancement is the consequence of a positive feedback of d-wave Cooper pairing on SDW correlations. As mentioned earlier, this is made possible by a k_{\perp} -dependent coupling of g_3 to normal scattering processes g_2 and g_1 . According to (B1), the first Fourier component in $\cos(k_{\perp 1}d_{\perp})\cos(k_{\perp 2}d_{\perp})$ of these couplings grows as temperature is lowered to finally become singular at the approach of T_c where $\chi_{\text{SCd}}(0)$ is divergent.

Anisotropy of umklapp scattering in momentum space along with its temperature dependence enter as key factors in the determination of resistivity at low temperature.

IV. NUMERICAL RESULTS FOR THE BOLTZMANN EQUATION

We can now proceed to the numerical solution of the linearized semi-classical Boltzmann equation (12), using (A6) and the above RG results for the renormalized umklapp vertex part. The solutions for the normalized functions $\bar{\phi}_{k_{\perp}}$ have been obtained for $N_P = 60$ patches for the Fermi surface sheet $\mathbf{k}_F^p(k_{\perp})$, which assures a convergence for the solutions of the Boltzmann equation (12) or (A6) that is independent of the discretization of the transverse Brillouin zone. Following (11), the temperature dependence of longitudinal resistivity can then be obtained by tuning the values of t_{\perp}' and initial g_3 .

A. Dimensionality of the electron gas and resistivity

We first consider in Fig. 4 the general features of longitudinal resistivity over the whole temperature interval. This includes the high - effectively 1D - temperature domain at $T > t_{\perp}$, its crossover to the 2D region at $T < t_{\perp}$ where the warping of the Fermi surface becomes quantum mechanically coherent, and finally the temperature domain $T_{\mu} < T < t_{\perp}'$ where antinesting effects come into play at the approach of instabilities.

From the Figure 4, we see that in the 1D temperature region of both SDW and SCd sectors of the phase diagram, the resistivity is not metallic but grows with decreasing temperature. This is the result of relevant umklapp scattering whose flow in the 1D domain is characterized by essentially no k_{\perp} dependence, that is, no transverse correlations, as illustrated in Fig. 2-b (top panel). The growth completely overcomes the linear T -resistivity decrease obtained in the limit of a constant g_3 (continuous line of Fig. 4). This insulating behaviour is consistent with previous 1D results obtained at half-filling^{37,38}.

When $t_{\perp}' < T < t_{\perp}$, the system crossovers to its 2D regime with antinesting effects remaining weak. In this temperature domain, the relevance of g_3 is still strong enough to outweigh the crossover toward the low temperature Fermi liquid $T^2 \ln T$ -resistivity behaviour found at constant g_3 ^{12,13} (continuous line of Fig. 4). Resistivity remains insulating in this region. It is only when T is further lowered below t_{\perp}' that the anisotropic growth of g_3 is significantly damped. At $t_{\perp}' > t_{\perp}^*$, in the SCd sector where umklapp, though still increasing, is no longer singular at finite T , resistivity goes through a maximum at $T \sim t_{\perp}'$ and is followed at lower temperature by a metallic behaviour. Metallic behaviour is also possible above T_{SDW} in the SDW sector of the phase diagram provided t_{\perp}' is relatively close to the critical t_{\perp}^* , as portrayed in Fig. 4. As we will show next, however, metallicity is in general not equivalent to a Fermi liquid behaviour. Deviations from the latter are found and correlated to the distance from t_{\perp}^* ; it is only at strong $t_{\perp}' \gg t_{\perp}^*$ that Fermi liquid features tend to be restored at sufficiently low temperature.

B. Resistivity at quantum criticality and beyond

We now focus on the low temperature profile of ρ_a at $T_{\mu} < T < t_{\perp}'$ on either side of the QCP t_{\perp}^* . Starting with the SDW side of the phase diagram, the Fig. 5 displays the temperature dependence of resistivity in the normal phase of the SDW instability at different t_{\perp}' and bare g_3 values. When t_{\perp}' is relatively far below t_{\perp}^* , resistivity remains insulating like with $d\rho_a/dT < 0$ down to T_{SDW} . The growth of umklapp scattering and therefore of SDW fluctuations is sufficiently strong to maintain the source of inelastic scattering and the insulating response of the electron gas. In these conditions, the behaviour varies

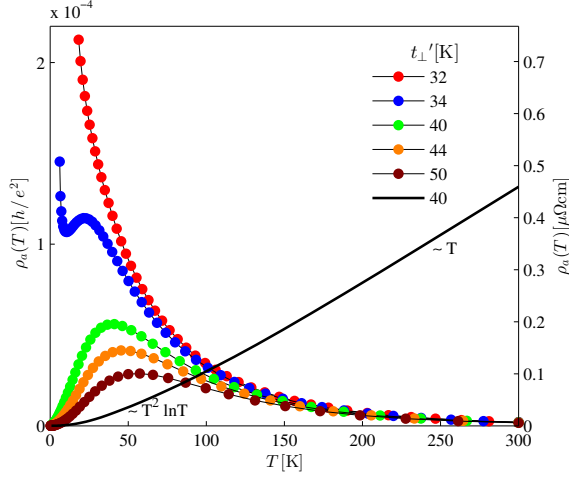


FIG. 4. (Color online) Calculated longitudinal resistivity over the whole temperature interval for different t'_{\perp} at $g_3 = 0.03$ ($t'_{\perp} = 38\text{K}$). The continuous line refers to the Fermi liquid limit at constant scale-independent $g_3 (= 0.03)$ yielding linear T -resistivity in the high temperature 1D domain ($T > t_{\perp}$) followed by a crossover toward a 2D $T^2 \ln T$ regime at low temperature.

weakly with the initial amplitude of g_3 .

The temperature profile of resistivity qualitatively change at the approach of t'_{\perp} . At $T \sim t'_{\perp}$, ρ_a reaches a maximum followed by a crossover to a metallic behaviour which persists down to very close to T_{SDW} . The singularity in umklapp, being still present despite sizeable nesting alterations, generates a resistivity upturn due to critical scattering, as meant in Figs 4 and 5. In the metallic regime, however, the resistivity deviates from the Fermi liquid prediction. A suitable way to describe these deviations is to express resistivity as a power law, $\rho_a(T) \sim T^{\alpha(T)}$, with a local exponent $\alpha(T)$ defined by

$$\alpha(T) = \frac{d}{d \ln T} \ln \rho_a(T). \quad (13)$$

The values of the exponent α are inserted in the calculated phase diagrams and shown in Fig. 7 for different bare amplitudes of g_3 . Thus in approaching t'_{\perp} from below the exponent $\alpha(T)$ crossovers from negative (insulating) to positive (metallic) values. Sufficiently close to t'_{\perp} , T_{SDW} is small and $\alpha(T)$ reaches unity for $T \lesssim 10\text{K}$, which corresponds to the linear- T resistivity usually associated to the QCP.

This linearity can be qualitatively understood if one considers that at low temperature resistivity is roughly speaking proportional to $T^2 \langle g_3^2 \rangle_{\text{FS}}$. This would indicate that the average of the square of umklapp scattering over the Fermi surface, $\langle g_3^2 \rangle_{\text{FS}} \sim 1/T$, essentially grows as the inverse of temperature above the transition. Note that this temperature dependence is similar to the SDW susceptibility that goes like $\chi_{\text{SDW}} \sim 1/T$ at $T \gg |\Theta|$ in this region^{20,22}.

If we now consider the SCd region at $t'_{\perp} \geq t'_{\perp}$, the

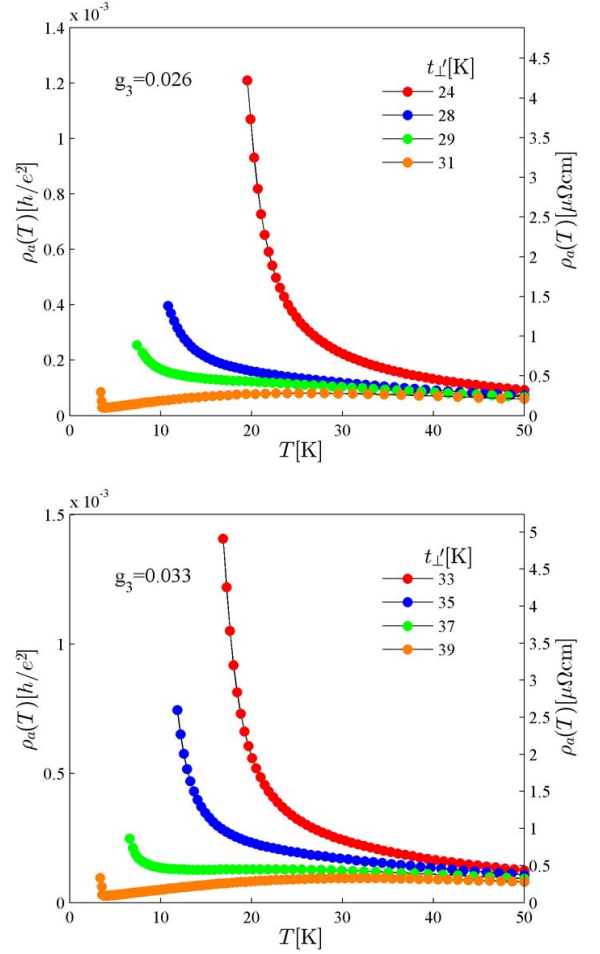


FIG. 5. (Color in line) Calculated resistivity at low temperature in the SDW domain of the phase diagram for different t'_{\perp} and g_3 .

linearity continues to be seen over a finite region of the phase diagram. From Figures 6 and 7, it can be found over a large temperature interval above T_c near t'_{\perp} . However, a shift in the value of $\alpha(T)$ toward larger values takes place at low enough temperature especially if g_3 is relatively small initially. As a function of temperature a fan shape like region then unfolds from the neighbourhood of t'_{\perp} in which $\alpha(T) \simeq 1$. This region of linear resistivity in the phase diagram broadens as the bare g_3 increases and spin fluctuations in the normal phase and then T_c are enhanced. Thus contrary to the situation expected for a classical QCP tied to SDW ordering alone³⁹, this region of linearity is not quickly followed as a function of t'_{\perp} by a T^2 -resistivity. The crossover region $1 < \alpha(T) < 2$ where deviations are present is rather wide and covers the whole region where superconductivity is present, as portrayed in Figure 7 for different g_3 . It is only in the low temperature domain close to T_c and for t'_{\perp} well above t'_{\perp} that the boundary with the Fermi liquid limit appears and T^2 -resistivity becomes visible (see Figures 6 and 7), namely where $\langle g_3^2 \rangle_{\text{FS}}$ becomes es-

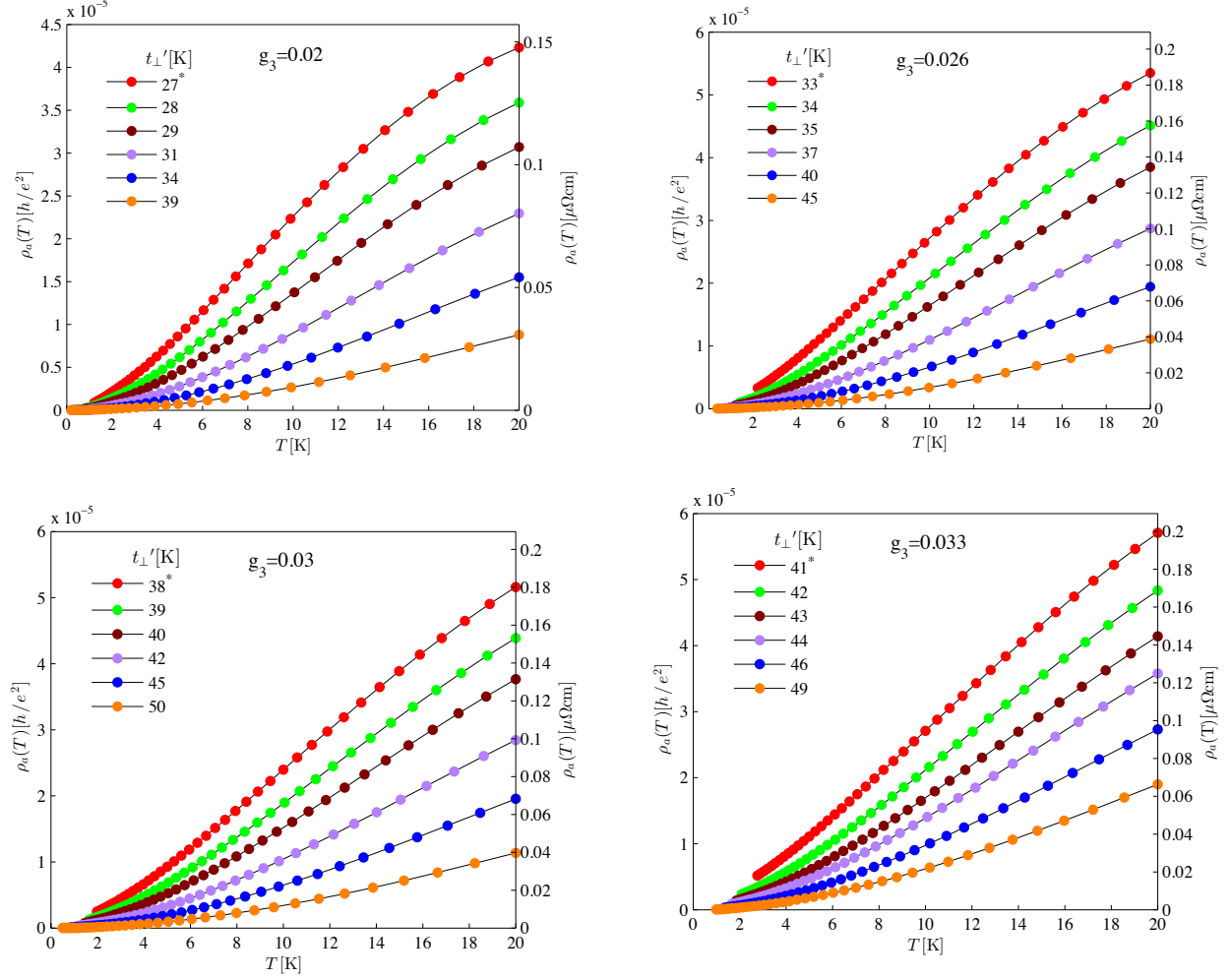


FIG. 6. (Color online) Calculated resistivity at low temperature in the SCd domain of the phase diagram for different t'_\perp and g_3 .

entially temperature independent. Similar features were found in previous RG calculations of the electron-electron scattering rate that included both normal and umklapp processes²². These were attributed to the presence of the superconducting instability that still influence the growth of the coupling constants; it gives rise to a positive feedback of SCd pairing on umklapp scattering which can account for this extended quantum critical behaviour.

C. Anisotropy of the scattering rate

It is instructive to extract from the above results for resistivity some information about the momentum resolved - k_\perp -dependent - scattering rate. According to (11), the conductivity $\sigma_a = \sum_i \sigma_{k_\perp i}$ is a sum of contributions coming from each patch. One can associate to each contribution a patch resistivity $\rho_{k_\perp i} = (\sigma_{k_\perp i})^{-1}$ as an element of an array of parallel resistors proportional to a scattering rate at $\mathbf{k}_F^p(k_\perp i)$ on the Fermi surface.

The Figure 8 shows the variation of $\rho_{k_\perp i}$ as a function of k_\perp . In the SCd regime, there are peaks at $k_\perp = 0$ and $\pm\pi$ indicating that the scattering rate is larger at these points. These warmer regions of scattering are the same as those of umklapp scattering amplitude along the Fermi surface in Fig. 3 and then differ from the positions $k_\perp = \pm\pi/4$ and $\pm3\pi/4$ attributed to the best nesting conditions for the spectrum. The resulting momentum profile of $\rho_{k_\perp i}$ over the Fermi surface is also congruent with the one previously found by a direct RG calculation of the scattering rate from the one-particle self-energy at low temperature, which takes into account both normal and umklapp processes²². As stressed in Ref.²² these warmer regions of scattering turn out to coincide with the locations of the maximum for a d-wave gap along the Fermi surface. Since a single scattering channel (Peierls) calculation would invariably leads to the best nesting points as the warmest spots of scattering on the Fermi surface, it follows that one can ascribe the shift in the spots on the Fermi surface to the presence of the interfer-

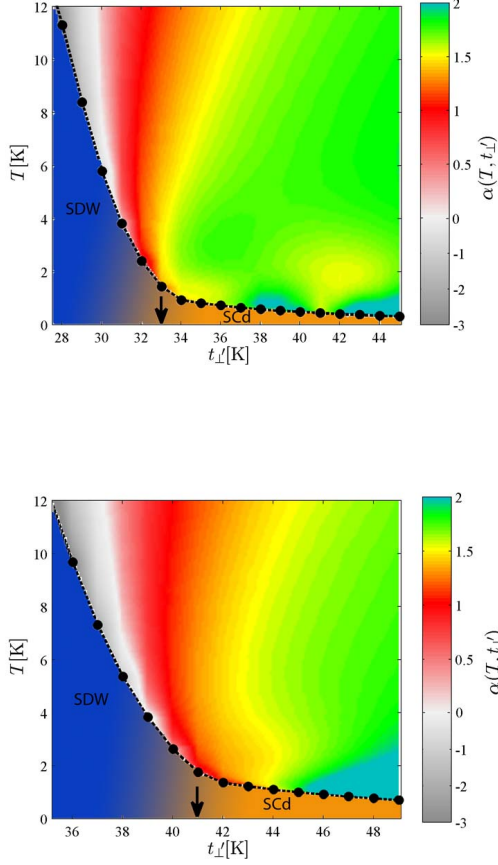


FIG. 7. (Color online) Variation of the power law exponent α of resistivity in the phase diagram for $g_3 = 0.026$ (top) and $g_3 = 0.033$ (bottom). The arrows indicate the location of t_{\perp}^* .

ing Cooper channel in the complete one-loop calculation (B1). The interference between both scattering channels being present in the SDW sector of the phase diagram as well, the anisotropy of $\rho_{k_{\perp}}$ is found to be similar above T_{SDW} , as displayed in Fig. 8.

D. Comparison with experiments

In the following we shall make some comparison of the above results with experiments. Starting with the SDW sector of the calculated phase diagram at low nesting deviations, the results displayed in Figures 4 and 5 show the absence of metallic resistivity above T_{SDW} . This is at variance to what is actually observed in system like $(\text{TMTSF})_2\text{PF}_6$ series of the Bechgaard salts series below P_c where a nearly T^2 behaviour for resistivity is well known to be observed above the resistivity upturn at $T_{\text{SDW}} \sim 10\text{K}^{10,28,40,41}$ (see also Fig. 9). The temperature profile obtained for resistivity well below t_{\perp}^* is rather characteristic of the one seen in the cousin sulfur

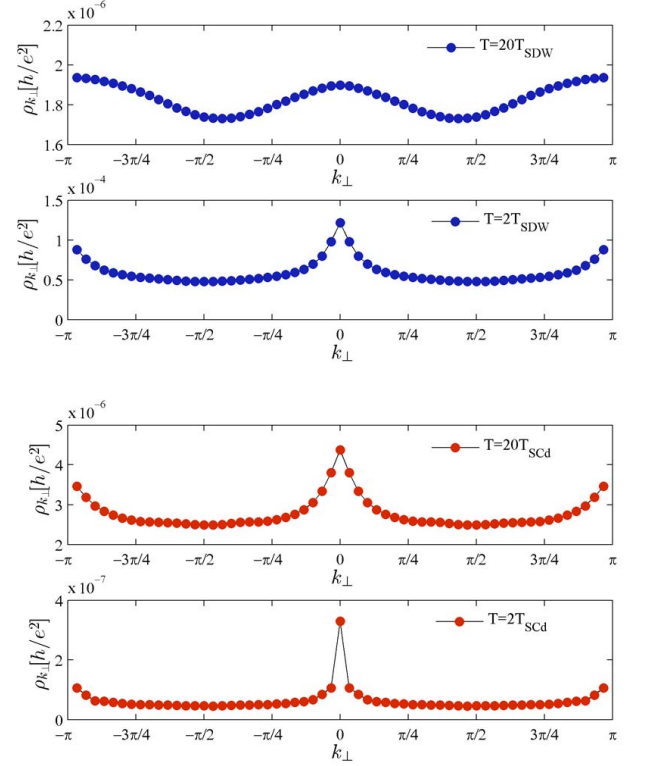


FIG. 8. (Color online) Variation of resistivity components along the Fermi surface at different temperatures: SDW (top) and SCd (bottom) domains.

based compounds $(\text{TMTTF})_2\text{X}$ ($\text{X}=\text{PF}_6, \text{Br}, \dots$) at low pressure⁴², which are characterized by a 1D Mott insulating gap at high temperature due to umklapp scattering, followed at lower temperature by a transition to an antiferromagnetic ground state^{27,28,43}. Under moderate pressure, the normal phase of these systems becomes metallic with a power law behaviour down to T_{SDW} which would agree qualitatively with the calculated positive values for α found at low temperature not too far below t_{\perp}^* in Figure 7. However in contrast to the results shown in Fig. 5, no maximum in resistivity is found experimentally for longitudinal resistivity at a scale that would correspond to t_{\perp}^* ²⁸. These discrepancies provide some indication that inelastic scattering at intermediate temperature and above would come from processes other than half-filling umklapp^{44–46}.

On the SC side, above the QCP at P_c , detailed resistivity measurements for $(\text{TMTSF})_2\text{PF}_6$ have been performed in the low temperature domain up to about 15 times T_c (T_c of the order of 1 K at P_c)^{10,11}. The resistivity data are reproduced in Figure 9. At the pressure of 11.8 kbar, close to the $P_c \simeq 9\text{kbar}$, resistivity is found to be T -linear ($\alpha = 1$) from up to $10T_c$ down to T_c and even below when a small magnetic field is applied, as shown in the log-log plot of Figure 9-b. As pressure is increased, the linearity decreases in strength and the resis-

tivity develops some upward curvature which translates into a gradual increase of the power law exponent α , but which still remains smaller than the Fermi liquid limit $\alpha = 2$. It is only at much larger pressure ($P = 20.8$ kbar in Fig. 9), when T_c becomes small, that the T^2 behaviour tends to be retrieved as shown in Fig. 9-b. Deviations to the Fermi liquid behaviour were found to scale with the size of $T_c^{10,11}$.

These features are consistent with the results of Fig. 7 where deviations from linearity develop with increasing the antinesting parameter so that the resistivity exponent reaches 2 when the superconducting phase is about to disappear. The calculated evolution of the exponent α near t_{\perp}^* and above is in qualitative agreement with the results of Fig. 9.

The theory, however, fails to predict the restoration of an apparent Fermi liquid T^2 -behaviour in the intermediate temperature region, namely above the domain of anomalous resistivity. As mentioned above, this Fermi liquid behaviour is also found in the SDW sector of the phase diagram above $T_{SDW} \sim 10$ K (see Fig. 9). In the present approach, this would indicate that the system crosses over to a state where umklapp renormalization becomes essentially absent, in spite of reinforced nesting properties resulting from either a temperature increase or a reduction of t_{\perp}^* . These features are at variance with the results of the present model that invariably predicts the reverse. For systems like the Bechgaard salts with one type of carriers tied to a single component Fermi surface, these features may indicate that a ‘colder’ source of inelastic scattering⁴⁷, not included in the present calculations, gains in importance at higher temperature. It surpasses around 10 K the anomalous power-law behaviour resulting from the sole basis of electronic half-filled umklapp scattering. This is also inferred from the calculated values of 3D resistivity for the present model. The actual resistivity is obtained from the product of the 2D part by the interchain lattice constant c , namely $\rho_a c$. For the Bechgaard salts, $c = 13.52 \text{ \AA}^2$ and the resistivity can then be expressed in $\mu\Omega \cdot \text{cm}$ units, as shown in the right-hand side scale of Figures 4-6. The comparison with the Fig. 9-b for the inelastic part of resistivity indicates that the data reach one order of magnitude larger values at 10 K, that is where the change of regime occurs (see Fig. 9).

V. SUMMARY AND CONCLUDING REMARKS

We have studied the temperature and pressure dependence of electrical resistivity of the Bechgaard salts quasi-one dimensional organic superconductors in the vicinity of their quantum critical point where superconductivity borders on spin-density-wave order under pressure. We have proceeded to the numerical solution of the semiclassical Boltzmann equation in which the collision umklapp electronic term has been computed by one-loop RG

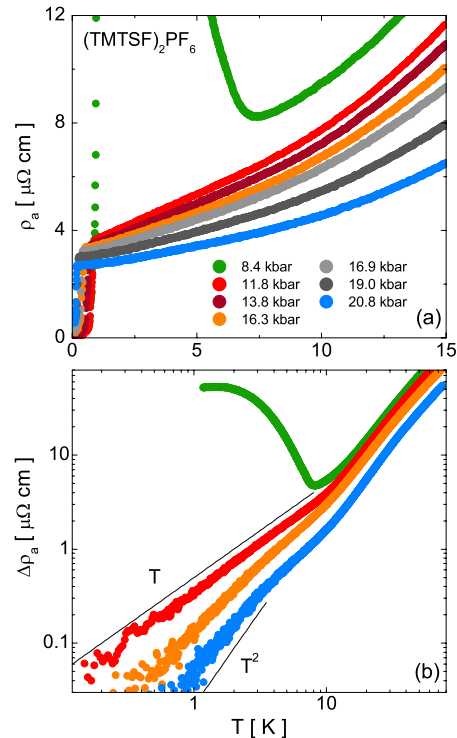


FIG. 9. (Color online) (a): Longitudinal resistivity of Ref.¹⁰ observed at different pressures or T_c for $(\text{TMTSF})_2\text{PF}_6$; (b): Inelastic part of the data ($\Delta\rho_a = \rho_a - \rho_a^0$) traced in a log-log plot showing the growth of the power law exponent α for resistivity with pressure.

calculations in the framework of the quasi-1D electron gas model in the presence of tunable nesting alterations.

The temperature dependence of longitudinal resistivity ρ_a has thus been obtained over the whole temperature domain from the 1D high temperature region, which is invariably insulating, down to the different effective 2D regimes where either an insulating SDW or SCd instabilities are found depending on the strength of antinesting parameter t_{\perp}^* . Antinesting proves to be the characteristic scale of the model for weakening the growth of umklapp term under scaling, allowing the onset of anomalous metallic resistivity near the quantum critical point t_{\perp}^* along the antinesting axis. Marked deviations from the Fermi liquid T^2 -behaviour have been found and described in terms of power law resistivity $\rho_a \sim T^\alpha$ in the chain direction. Linear resistivity is found within a characteristic fan shape region of the phase diagram near t_{\perp}^* , followed by a gradual increase of the exponent α , reaching the Fermi liquid limit at low enough temperature and sufficiently large antinesting or low superconducting T_c .

Quantum critical regime can be understood as an anomalous increase of umklapp scattering with lower-

ing temperature, an enhancement that turns out to be non uniform or anisotropic along the Fermi surface, with peaks at the positions where the Fermi velocity is purely longitudinal and nesting is relatively poor. This umklapp vertex renormalization being directly linked to an enhancement of SDW correlations, these can be equivalently considered as the source of anomalous inelastic scattering. The region of non Fermi liquid values of α are found to extend well beyond the confines of the QCP vicinity, a consequence of the reinforcement of umklapp scattering or SDW fluctuations by d-wave Cooper pairing. This leads to the apparent correlation of α with the size of T_c .

The results have been shown to qualitatively account for the linear- T longitudinal resistivity observed near the QCP of the Bechgaard salts phase diagram and for the gradual growth of α toward the Fermi liquid behaviour, as pressure moves away from the QCP and T_c is suppressed. However, discrepancies between theory and experiment remain. The present approach to resistivity fails to reproduce the crossover to an apparent Fermi liquid in the intermediate temperature domain, namely above that of quantum critical effects. For systems like the Bechgaard salts with a simple open Fermi surface, this is likely to point to a mechanism of electron scattering that superimposes to that of half-filling umklapp with increasing temperature.

ACKNOWLEDGMENTS

The authors would like to thank H. Bakrim for his valuable comments on computing aspects of this work, and N. Doiron-Leyraud and P. Auban-Senzier for sharing their experimental data on the resistivity of the Bechgaard salts. C. B. thanks the National Science and Engineering Research Council of Canada (NSERC) and the Réseau Québécois des Matériaux de Pointe (RQMP) for financial support. Computational resources were provided by the Réseau québécois de calcul de haute performance (RQCHP) and Compute Canada.

Appendix A: The linearized Boltzmann equation

The linearized Boltzmann equation is of the form

$$\sum_{i, \mathbf{k}'} \mathcal{L}_{\mathbf{k}, \mathbf{k}'}^{[i]} \phi_{\mathbf{k}'} = e\beta \mathcal{E} \cdot v_{\mathbf{k}}, \quad (\text{A1})$$

where the collision operator given by expression (9) is the sum of four terms

$$\begin{aligned} \sum_{i=1}^4 \mathcal{L}_{\mathbf{k}, \mathbf{k}'}^{[i]} &= \frac{1}{(LN_P)^2} \sum_{\mathbf{k}_2, \mathbf{k}_3, \mathbf{k}_4} \frac{1}{2} |g_3(k_{\perp}, k_{\perp 2}, k_{\perp 3}, k_{\perp 4}) - g_3(k_{\perp}, k_{\perp 2}, k_{\perp 4}, k_{\perp 3})|^2 \times \frac{2\pi}{\hbar} \delta_{\mathbf{k}+\mathbf{k}_2, \mathbf{k}_3+\mathbf{k}_4+p} \mathbf{G} \\ &\times \delta(\varepsilon_{\mathbf{k}}^p + \varepsilon_{\mathbf{k}_2}^{p_2} - \varepsilon_{\mathbf{k}_3}^{p_3} - \varepsilon_{\mathbf{k}_4}^{p_4}) \frac{f^0(\mathbf{k}_2)[1 - f^0(\mathbf{k}_3)][1 - f^0(\mathbf{k}_4)]}{[1 - f^0(\mathbf{k})]} (\delta_{\mathbf{k}, \mathbf{k}'} + \delta_{\mathbf{k}_2, \mathbf{k}'} - \delta_{\mathbf{k}_3, \mathbf{k}'} - \delta_{\mathbf{k}_4, \mathbf{k}'}). \quad (\text{A2}) \end{aligned}$$

In the framework of the electron gas model, we have used

$$\langle \mathbf{k}_1, \mathbf{k}_2 | g_3 | \mathbf{k}_3, \mathbf{k}_4 \rangle = \pi \hbar v_F g_3(k_{\perp 1}, k_{\perp 2}, k_{\perp 3}, k_{\perp 4})$$

for the (normalized) umklapp vertex functions evaluated on the Fermi surface. By separating the kinematics constraint on the momentum conservation into its longitudinal and transverse components¹², one has

$$\begin{aligned} \delta_{\mathbf{k}+\mathbf{k}_2, \mathbf{k}_3+\mathbf{k}_4+p} \mathbf{G} &= \delta_{k_{\perp}+k_{\perp 2}, k_{\perp 3}+k_{\perp 4}} \\ &\times \frac{2\pi}{L} \hbar v_F \delta(\varepsilon_{\mathbf{k}}^p + \varepsilon_{\mathbf{k}_2}^{p_2} + \varepsilon_{\mathbf{k}_3}^{p_3} + \varepsilon_{\mathbf{k}_4}^{p_4} - \Sigma), \quad (\text{A3}) \end{aligned}$$

where $\Sigma = \varepsilon_{\perp}(k_{\perp}) + \varepsilon_{\perp}(k_{\perp 2}) + \varepsilon_{\perp}(k_{\perp 3}) + \varepsilon_{\perp}(k_{\perp 4})$.

The summation over the momentum vectors can be written as

$$\frac{1}{LN_P} \sum_{\mathbf{k}} = \sum_p \int \frac{d\varepsilon_{\mathbf{k}}^p}{2\pi \hbar v_F} \frac{1}{N_P} \sum_{k_{\perp}}. \quad (\text{A4})$$

Carrying out the integration over the energy variables $(\varepsilon_{\mathbf{k}_3}^{p_3}, \varepsilon_{\mathbf{k}_4}^{p_4})$ and $(\varepsilon_{\mathbf{k}_2}^{p_2}, \varepsilon_{\mathbf{k}_4}^{p_4})$ for respectively the first and the last two terms of (A2), we arrive at the corresponding expressions entering the collision operator,

$$\begin{aligned}
\mathcal{L}_{\mathbf{k},\mathbf{k}'}^{[1]} &= \frac{\pi^2}{\hbar N_P^2} \sum_{k_{\perp 3}, k_{\perp 4}} |g_3(k_{\perp}, k_{\perp 3} + k_{\perp 4} - k_{\perp}, k_{\perp 3}, k_{\perp 4}) - g_3(k_{\perp}, k_{\perp 3} + k_{\perp 4} - k_{\perp}, k_{\perp 4}, k_{\perp 3})|^2 \\
&\quad \times \frac{1 + e^{-\beta \varepsilon_{\mathbf{k}}^p}}{1 + e^{\beta(\Sigma/2 - \varepsilon_{\mathbf{k}}^p)}} \frac{\Sigma/2 e^{\beta \Sigma/2}}{e^{\beta \Sigma/2} - 1} \delta_{\mathbf{k},\mathbf{k}'}, \\
\mathcal{L}_{\mathbf{k},\mathbf{k}'}^{[2]} &= \frac{\pi^3 v_F}{L N_P^2} \sum_{k_{\perp 3}, k_{\perp 4}} |g_3(k_{\perp}, k'_{\perp}, k_{\perp 3}, k_{\perp 4}) - g_3(k_{\perp}, k'_{\perp}, k_{\perp 4}, k_{\perp 3})|^2 \\
&\quad \times \delta_{k_{\perp} + k'_{\perp}, k_{\perp 3} + k_{\perp 4}} \delta(\varepsilon_{\mathbf{k}}^p + \varepsilon_{\mathbf{k}'}^{p'} - \Sigma_1/2) \frac{1 + e^{-\beta \varepsilon_{\mathbf{k}}^p} (\varepsilon_{\mathbf{k}}^p + \varepsilon_{\mathbf{k}'}^{p'}) e^{\beta(\varepsilon_{\mathbf{k}}^p + \varepsilon_{\mathbf{k}'}^{p'})}}{1 + e^{\beta \varepsilon_{\mathbf{k}'}^{p'}}} \frac{e^{\beta(\varepsilon_{\mathbf{k}}^p + \varepsilon_{\mathbf{k}'}^{p'})}}{e^{\beta(\varepsilon_{\mathbf{k}}^p + \varepsilon_{\mathbf{k}'}^{p'})} - 1}, \\
\mathcal{L}_{\mathbf{k},\mathbf{k}'}^{[3]} &= -\frac{\pi^3 v_F}{L N_P^2} \sum_{k_{\perp 2}, k_{\perp 4}} |g_3(k_{\perp}, k_{\perp 2}, k'_{\perp}, k_{\perp 4}) - g_3(k_{\perp}, k_{\perp 2}, k_{\perp 4}, k'_{\perp})|^2 \\
&\quad \times \delta_{k_{\perp} + k_{\perp 2}, k'_{\perp} + k_{\perp 4}} \frac{1 + e^{-\beta \varepsilon_{\mathbf{k}}^p}}{1 + e^{-\beta \varepsilon_{\mathbf{k}'}^{p'}}} \frac{1}{(e^{\beta(\Sigma_2/2 - \varepsilon_{\mathbf{k}}^p)} + 1)(e^{-\beta(\Sigma_2/2 - \varepsilon_{\mathbf{k}'}^{p'})} + 1)}, \\
\mathcal{L}_{\mathbf{k},\mathbf{k}'}^{[4]} &= -\frac{\pi^3 v_F}{L N_P^2} \sum_{k_{\perp 2}, k_{\perp 3}} |g_3(k_{\perp}, k_{\perp 2}, k_{\perp 3}, k'_{\perp}) - g_3(k_{\perp}, k_{\perp 2}, k'_{\perp}, k_{\perp 3})|^2 \\
&\quad \times \delta_{k_{\perp} + k_{\perp 2}, k_{\perp 3} + k'_{\perp}} \frac{1 + e^{-\beta \varepsilon_{\mathbf{k}}^p}}{1 + e^{-\beta \varepsilon_{\mathbf{k}'}^{p'}}} \frac{1}{(e^{\beta(\Sigma_3/2 - \varepsilon_{\mathbf{k}}^p)} + 1)(e^{-\beta(\Sigma_3/2 - \varepsilon_{\mathbf{k}'}^{p'})} + 1)}, \tag{A5}
\end{aligned}$$

where Σ_1 , Σ_2 , and Σ_3 are obtained by substituting respectively $k_{\perp 2}$, $k_{\perp 3}$, and $k_{\perp 4}$ with k'_{\perp} in the Σ expression.

The normalized equation to solve numerically for the ϕ' s reads

$$\sum_{i,\mathbf{k}'} \tilde{\mathcal{L}}_{\mathbf{k},\mathbf{k}'}^{[i]} \bar{\phi}_{\mathbf{k}'} = 1,$$

where according to (A1) we have defined the normalized quantities $\pi d_{\perp} \mathcal{L}^{[i]}/v_F \rightarrow \tilde{\mathcal{L}}^{[i]}$ and $\phi/(e \mathcal{E}_a \beta d_{\perp}) \rightarrow \bar{\phi}$. Carrying out the integration over $\varepsilon_{\mathbf{k}'}^{p'}$ and rearranging the terms we arrive at the final equation,

$$\begin{aligned}
&\frac{\pi^3 d_{\perp}}{2a} \frac{T}{E_F} \frac{1}{N_P^2} \sum_{k'_{\perp}, k_{\perp 3}, k_{\perp 4}} \left\{ |g_3(k_{\perp}, k_{\perp 3} + k_{\perp 4} - k_{\perp}, k_{\perp 3}, k_{\perp 4}) - g_3(k_{\perp}, k_{\perp 3} + k_{\perp 4} - k_{\perp}, k_{\perp 4}, k_{\perp 3})|^2 \frac{\beta \Sigma'/2}{\sinh(\beta \Sigma'/2)} \delta_{k_{\perp}, k'_{\perp}} \right. \\
&+ |g_3(k_{\perp}, k'_{\perp}, k_{\perp 3}, k_{\perp 4}) - g_3(k_{\perp}, k'_{\perp}, k_{\perp 4}, k_{\perp 3})|^2 \frac{\beta \Sigma''/2}{\sinh(\beta \Sigma''/2)} \delta_{k_{\perp} + k'_{\perp}, k_{\perp 3} + k_{\perp 4}} \\
&- 2 |g_3(k_{\perp}, k_{\perp 3}, k'_{\perp}, k_{\perp 4}) - g_3(k_{\perp}, k_{\perp 3}, k_{\perp 4}, k'_{\perp})|^2 \frac{\beta \Sigma''/2}{\sinh(\beta \Sigma''/2)} \delta_{k_{\perp} + k_{\perp 3}, k'_{\perp} + k_{\perp 4}} \left. \right\} \bar{\phi}_{k'_{\perp}} = 1, \tag{A6}
\end{aligned}$$

where

$$\begin{aligned}
\Sigma' &= \epsilon_{\perp}(k_{\perp}) + \epsilon_{\perp}(k_{\perp 3} + k_{\perp 4} - k_{\perp}) + \epsilon_{\perp}(k_{\perp 3}) + \epsilon_{\perp}(k_{\perp 4}), \\
\Sigma'' &= \epsilon_{\perp}(k_{\perp}) + \epsilon_{\perp}(k'_{\perp}) + \epsilon_{\perp}(k_{\perp 3}) + \epsilon_{\perp}(k_{\perp 4}). \tag{A7}
\end{aligned}$$

We shall fix the ratio $d_{\perp}/a \simeq 1.05$ in (A6) from the known values of lattice constants in the Bechgaard salts for the longitudinal \hat{a} (7.3Å) and transverse \hat{b} (7.7Å) directions². The solution of (A6) for the $\phi_{k_{\perp}}$ on the Fermi surface leads to the evaluation of conductivity (11) as the inverse of resistivity.

Appendix B: One-loop renormalization group for the electron gas

1. Vertices

The renormalization group approach to the quasi-1D electron gas is detailed in Refs²⁰⁻²². In the outline, the method starts with the segmentation of energy shells of thickness $\frac{1}{2}E_0(\ell)d\ell$, located at $\pm \frac{1}{2}E_0(\ell)$ from either sides of the Fermi sheets, into N_p patches, each centred at a particular value of the transverse momentum k_{\perp} , where $E_0(\ell) = E_0 e^{-\ell}$ is the scaled bandwidth at step ℓ and $E_0 \equiv 2E_F$ is the initial bandwidth. The successive partial trace integration of electron degrees of freedom in the partition function leads to the renormalization or

flow of the scattering amplitudes g_i as a function of ℓ . At the one-loop level, the flow combines corrections from

the electron-hole (Peierls) and electron-electron (Cooper) interfering channels of scattering and leads to the flow equations written in the compact form

$$\begin{aligned}\partial_\ell g_1(k_{\perp 1}, k_{\perp 2}, k_{\perp 3}, k_{\perp 4}) &= (-2g_1 \circ g_1 + g_1 \circ g_2 + g_2 \circ g_1) \partial_\ell \mathcal{L}_P - (g_1 \circ g_2 + g_2 \circ g_1) \partial_\ell \mathcal{L}_C, \\ \partial_\ell g_2(k_{\perp 1}, k_{\perp 2}, k_{\perp 3}, k_{\perp 4}) &= -(g_1 \circ g_1 + g_2 \circ g_2) \partial_\ell \mathcal{L}_C + (g_2 \circ g_2 + g_3 \circ g_3) \partial_\ell \mathcal{L}_P, \\ \partial_\ell g_3(k_{\perp 1}, k_{\perp 2}, k_{\perp 3}, k_{\perp 4}) &= (-g_1 \circ g_3 - g_3 \circ g_1 + g_2 \circ g_3 + g_3 \circ g_2) \partial_\ell \mathcal{L}_P + 2g_2 \bullet g_3 \partial_\ell \mathcal{L}_P,\end{aligned}\quad (\text{B1})$$

where $\partial_\ell = \partial/\partial\ell$. $\mathcal{L}_{\nu=P,C}$ are the Peierls and Cooper loops whose derivative at finite temperature comprises an integration over the patch. These take the form

$$\begin{aligned}\partial_\ell \mathcal{L}_\nu(k_\perp, q_{\perp\nu}^{(\prime)}) &= \frac{E_0(\ell)}{4N_P} \sum_{\mu=\pm 1} \int_{k_\perp - \frac{\pi}{N_P}}^{k_\perp + \frac{\pi}{N_P}} \frac{dk_\perp}{2\pi} \\ &\times \frac{\theta(|E_0(\ell)/2 + \mu A_\nu| - E_0(\ell)/2)}{E_0(\ell) + \mu A_\nu} \\ &\times \left[\tanh[\beta E_0(\ell)/4] + \tanh[\beta(E_0(\ell)/4 + \mu A_\nu/2)] \right],\end{aligned}\quad (\text{B2})$$

where

$$\begin{aligned}A_\nu(k_\perp, q_{\perp\nu}^{(\prime)}) &= -\epsilon_\perp(k_\perp) - \eta_\nu \epsilon_\perp(\eta_\nu k_\perp + q_{\perp\nu}^{(\prime)}) \\ &+ \eta_\nu \epsilon_\perp(\eta_\nu k_{\perp 2(4)} + q_{\perp\nu}^{(\prime)}) + \epsilon_\perp(k_{\perp 2(4)})\end{aligned}\quad (\text{B3})$$

with $q_{\perp P}^{(\prime)} = k_{\perp 3} - k_{\perp 2} = k_{\perp 1} - k_{\perp 4}$ ($k_{\perp 3} - k_{\perp 1} = k_{\perp 2} - k_{\perp 4}$) and $q_{\perp C}^{(\prime)} = k_{\perp 1} + k_{\perp 2} = k_{\perp 3} + k_{\perp 4}$; $\eta_P = 1$ and $\eta_C = -1$. $\theta(x)$ is the Heaviside function [$\theta(0) \equiv \frac{1}{2}$].

The momentum dependence of couplings in the discrete convolution products ‘ \circ ’ over the internal k_\perp loop variable on the right-hand side of (B1) are in order $g(k_\perp, k_{\perp 4}, k_{\perp 1}, k_\perp - q_{\perp P})g(k_\perp, k_{\perp 2}, k_{\perp 3}, k_\perp - q_{\perp P})$ for the Peierls channel, $g(k_{\perp 1}, k_{\perp 2}, k_\perp, q_{\perp C} - k_\perp)g(k_{\perp 3}, k_{\perp 4}, k_\perp, q_{\perp C} - k_\perp)$ for the Cooper channel, and $g(k_\perp, k_{\perp 4}, k_{\perp 2}, k_\perp - q_{\perp P})g(k_{\perp 1}, k_\perp, k_{\perp 3}, k_{\perp 1} - q_{\perp P})$ for the ‘ \bullet ’ product of the off-diagonal Peierls channel.

2. Susceptibilities

The linear response of the electron system to a source field of SDW and SCD order parameter leads to the corresponding expressions of the normalized static susceptibility

$$\bar{\chi}_\mu(\mathbf{q}_\mu) = 2 \int_\ell (f_\mu(k_\perp) z_\mu(k_\perp))^2 \partial_\ell \mathcal{L}_\mu d\ell \quad (\text{B4})$$

for $\mu = \text{SDW}$ at $\mathbf{q}_0 = (2k_F, \pi)$ and $\mu = \text{SCd}$ at $\mathbf{q}_0 = 0$. These are functions of the renormalization factor for the pair vertex z_μ in the corresponding channel which obeys the following flow equation

$$\partial_\ell z_\mu(k_\perp) = (\partial_\ell \mathcal{L}_\mu) g_\mu z_\mu(k'_\perp), \quad (\text{B5})$$

where

$$\begin{aligned}g_{\text{SDW}} &= g_2(k'_\perp + \pi, k_\perp, k_\perp + \pi, k'_\perp) \\ &+ g_3(k'_\perp - \pi, k_\perp + \pi, k_\perp, k'_\perp), \\ g_{\text{SCd}} &= -g_1(-k'_\perp, k'_\perp, -k_\perp, k_\perp) \\ &- g_2(-k'_\perp, k'_\perp, -k_\perp, k_\perp),\end{aligned}\quad (\text{B6})$$

are the combinations of momentum dependent scattering amplitudes that govern the flow for each susceptibility. The form factors f_μ assigned to the nature of ordered phases are $f_{\text{SDW}} = 1$ and $f_{\text{SCd}} = \sqrt{2} \cos k_\perp$.

* maryam.shahbazi@usherbrooke.ca

† claude.bourbonnais@USherbrooke.ca

¹ D. Jérôme, A. Mazaud, M. Ribault, and K. Bechgaard, J. Phys. (Paris) Lett. **41**, L95 (1980).

² D. Jérôme and H. J. Schulz, Adv. Phys. **31**, 299 (1982).

³ C. Bourbonnais and D. Jérôme, in *The Physics of Organic Superconductors and Conductors*, Vol. 110, Springer Series in Materials Science, edited by A. Lebed (Springer, Heidelberg, 2008) p. 357, see also arXiv:cond-mat/0904.0617.

⁴ S. E. Brown, Physica C **514**, 279 (2015).

⁵ L. Taillefer, Annu. Rev. Condens. Matter Phys. **1**, 51 (2010).

⁶ N. P. Armitage, P. Fournier, and R. L. Greene, Rev. Mod. Phys. **82**, 2421 (2010).

⁷ T. Tomita, K. Kuga, Y. Uwatoko, P. Coleman, and S. Nakatsuji, Science **349**, 506 (2015).

⁸ D. J. Scalapino, Rev. Mod. Phys. **84**, 1383 (2012).

⁹ G. R. Stewart, Rev. Mod. Phys. **83**, 1589 (2011).

¹⁰ N. Doiron-Leyraud, P. Auban-Senzier, S. René de Cotret, C. Bourbonnais, D. Jérôme, K. Bechgaard, and L. Taillefer, Phys. Rev. B **80**, 214531 (2009).

¹¹ N. Doiron-Leyraud, P. Auban-Senzier, S. R. de Cotret, C. Bourbonnais, A. Sedeki, D. Jérôme, K. Bechgaard, and L. Taillefer, Eur. Phys. J. B **78**, 23 (2010).

- ¹² L. P. Gorkov and M. Mochena, Phys. Rev. B **57**, 6204 (1998).
- ¹³ A. T. Zheleznyak and V. M. Yakovenko, Eur. Phys. J. B **11**, 385 (1999).
- ¹⁴ V. J. Emery, R. Bruinsma, and S. Barisic, Phys. Rev. Lett. **48**, 1039 (1982).
- ¹⁵ C. Bourbonnais, F. Creuzet, D. Jérôme, K. Bechgaard, and A. Moradpour, J. Phys. (Paris) Lett. **45**, L755 (1984).
- ¹⁶ F. Creuzet, C. Bourbonnais, L. G. Caron, D. Jérôme, and A. Moradpour, Synth. Met. **19**, 277 (1987).
- ¹⁷ W. Wu, P. M. Chaikin, W. Kang, J. Shinagawa, W. Yu, and S. E. Brown, Phys. Rev. Lett. **94**, 097004 (2005).
- ¹⁸ S. E. Brown, P. M. Chaikin, and M. J. Naughton, in *The Physics of Organic Superconductors and Conductors*, Vol. 110, Springer Series in Materials Science, edited by A. Lebed (Springer, Heidelberg, 2008) p. 49.
- ¹⁹ Y. Kimura, M. Misawa, and A. Kawamoto, Phys. Rev. B **84**, 045123 (2011).
- ²⁰ C. Bourbonnais and A. Sedeki, Phys. Rev. B **80**, 085105 (2009).
- ²¹ J. C. Nickel, R. Duprat, C. Bourbonnais, and N. Dupuis, Phys. Rev. B **73**, 165126 (2006).
- ²² A. Sedeki, D. Bergeron, and C. Bourbonnais, Phys. Rev. B **85**, 165129 (2012).
- ²³ H. Meier, P. Auban-Senzier, C. Pépin, and D. Jérôme, Phys. Rev. B **87**, 125128 (2013).
- ²⁴ J. M. Buhmann, M. Ossadnik, T. M. Rice, and M. Sigrist, Phys. Rev. B **87**, 035129 (2013).
- ²⁵ H. Haug and A. P. Jauho, in *Quantum Kinetics in Transport and Optics of Semiconductors*, Vol. 110, Springer Series in Solid-State Sciences, edited by M. Cardona and P. Fulde (Springer, Heidelberg, 2008) p. 3.
- ²⁶ P. Wzietek, F. Creuzet, C. Bourbonnais, D. Jérôme, K. Bechgaard, and P. Batail, J. Phys. I (France) **3**, 171 (1993).
- ²⁷ B. J. Klemme, S. E. Brown, P. Wzietek, P. B. G. Kriza, D. Jérôme, and J.-M. Fabre, Phys. Rev. Lett. **75**, 2408 (1995).
- ²⁸ J. Moser, M. Gabay, P. Auban-Senzier, D. Jérôme, K. Bechgaard, and J. M. Fabre, Eur. Phys. J. B **1**, 39 (1998).
- ²⁹ P. M. Grant, J. Phys. (Paris) Coll. **44**, 847 (1983).
- ³⁰ S. Barisic and S. Brazovskii, in *Recent Developments in Condensed Matter Physics*, Vol. 1, edited by J. T. Devreese (Plenum, New York, 1981) p. 327.
- ³¹ F. Mila and K. Penc, Phys. Rev. B **50**, 11429 (1994).
- ³² P. M. Grant, Phys. Rev. B **26**, 6888 (1982).
- ³³ L. Ducasse, A. Abderrabba, and B. Gallois, J. Phys. C **18**, L947 (1985).
- ³⁴ C. Bourbonnais and L. G. Caron, Int. J. Mod. Phys. B **05**, 1033 (1991).
- ³⁵ C. Bourbonnais, B. Guay, and R. Wortis, in *Theoretical methods for strongly correlated electrons*, edited by D. Sénéchal, A. M. Tremblay, and C. Bourbonnais (Springer, Heidelberg, 2003) pp. 77–78, arXiv: cond-mat/0204163.
- ³⁶ C. Bourbonnais and A. Sedeki, C. R. Physique **12**, 532 (2011).
- ³⁷ L. P. Gor'kov and I. E. Dzyaloshinskii, JETP Lett. **18**, 401 (1973).
- ³⁸ T. Giamarchi, Phys. Rev. B **44**, 2905 (1991).
- ³⁹ T. Moriya and K. Ueda, Rep. Prog. Phys. **66**, 1299 (2003).
- ⁴⁰ K. Bechgaard, C. Jacobsen, K. Mortensen, H. Pedersen, and N. Thorup, Solid State Comm. **33**, 1119 (1980).
- ⁴¹ T. Vuletic, P. Auban-Senzier, C. Pasquier, S. Tomic, D. Jerome, M. Heritier, and K. Bechgaard, Eur. Phys. J. B **25**, 319 (2002).
- ⁴² C. Coulon, P. Delhaes, S. Flandrois, R. Lagnier, E. Bonjour, and J. Fabre, J. Phys. (Paris) **43**, 1059 (1982).
- ⁴³ L. Balicas, K. Benhia, W. Kang, E. Canadell, M. R. P. Auban-Senzier, D. Jérôme, and J. Fabre, J. Phys. I (France) **4**, 1539 (1994).
- ⁴⁴ T. Giamarchi, Physica **B230-232**, 975 (1997).
- ⁴⁵ A. Schwartz, M. Dressel, G. Grüner, V. Vescoli, L. Degiorgi, and T. Giamarchi, Phys. Rev. B **58**, 1261 (1998).
- ⁴⁶ M. Tsuchiizu, H. Yoshioka, and Y. Suzumura, J. Phys. Soc. Jpn. **70**, 1460 (2001).
- ⁴⁷ R. Hlubina and T. M. Rice, Phys. Rev. B **51**, 9253 (1995).